



Spatial and anchoring effects of zirconia-doped 3D scaffolds for stable zinc anodes

Jinxiu Ye^a, Tiancheng Ge^a, Xin Qu^a, Mohamedazeem M. Mohideen^a, Ce Wang^b, Ping Hu^c, Yong Liu^{a,*}

^a Beijing Key Laboratory of Advanced Functional Polymer Composites, College of Material Science and Engineering, Beijing University of Chemical Technology, Beijing 100029, China

^b Alan G. MacDiarmid Institute, Jilin University, Changchun, Jilin 130012, China

^c Department of Chemical Engineering, Tsinghua University, Beijing 100084, China

ARTICLE INFO

Keywords:

Aqueous Zinc-Ion Batteries
Carbon Nanofiber
Dendrite growth
Spatial Effect
Anchoring Effect

ABSTRACT

Dendrite growth and polarization are significant obstacles to the cycling stability of aqueous zinc-ion batteries (AZIBs). This work reports a zirconia-doped carbon nanofiber (ZrO₂-CF) 3D scaffold fabricated via electrospinning and thermal treatment. Through electrochemical testing, physical characterization, first-principles calculations, and finite element simulations, we analyzed the structure, mechanism, and performance of ZrO₂-CF as a modified anode material. The unique 3D architecture of ZrO₂-CF induces a “spatial effect,” offering a high specific surface area and excellent electronic pathways. Additionally, the “anchoring effect” of ZrO₂, nitrogen-containing groups, and C—O—Zr and N—Zr—O bridges promotes uniform Zn deposition, enhances interfacial stability, and suppresses hydrogen evolution. The ZrO₂-CF electrode achieves a high Coulombic efficiency of 98.6 % over 100 cycles and, in full cell, delivers initial capacities of 75 mAh g⁻¹ at 1,000 mA g⁻¹ and 124 mAh g⁻¹ at 200 mA g⁻¹, with retention rates of 47 % and 76.8 % after 100 cycles, respectively. This study demonstrates the synergistic effects of “spatial” and “anchoring” mechanisms in mitigating dendrite growth and polarization, highlighting the potential of ZrO₂-CF scaffolds for improving the overall performance of AZIBs.

1. Introduction

Aqueous rechargeable batteries (ARBs) have emerged as promising energy storage systems due to their inherent safety, affordability, and environmental compatibility [1,2]. Among ARBs, aqueous potassium-ion batteries (AKIBs) stand out for their fast ionic transport and high power densities due to the small Stokes radius of K⁺ [3]. However, the relatively low binding energy of K⁺ with host materials often leads to limited capacity and cycling stability [4,5]. Aqueous sodium-ion batteries (ASIBs) benefit from abundant sodium resources and low-cost scalability, yet their relatively large ionic radius hinders ion diffusion and leads to sluggish kinetics [6,7]. Aqueous lithium-ion batteries (ALIBs) deliver higher energy densities, but lithium scarcity and cost limit their widespread application [8,9]. Multivalent cation-based systems, such as aqueous magnesium-ion (AMIBs) [10], Aluminum-ion (AAIBs) [11] and calcium-ion (ACIBs) [12] batteries, offer higher volumetric capacities but suffer from sluggish ion diffusion, poor reversibility, and narrow electrochemical stability windows [13,14]. By

comparison, aqueous zinc-ion batteries (AZIBs) present a highly balanced alternative, combining the advantages of multivalent cations with scalability, safety, and material abundance [15,16]. Zinc metal, with its high theoretical capacity (820 mAh g⁻¹, 5855 mAh cm⁻³), low redox potential (−0.76 V vs. SHE), and established global reserves, offers a compelling solution for energy storage [17–19]. However, despite their balanced advantages, AZIBs are not without limitations. Key challenges include dendritic zinc growth, hydrogen evolution reactions (HER), and significant polarization effects, which compromise cycling stability, capacity retention, and safety [1,7,13]. These issues demand targeted solutions to unlock the full potential of AZIBs as a robust and scalable energy storage technology.

The dendritic growth of zinc during plating/stripping cycles is a critical issue. Uneven electric field distributions and localized zinc-ion concentration gradients lead to preferential deposition, evolving into dendritic structures. These dendrites risk puncturing the separator, causing short circuits and safety hazards. Detached zinc, or “dead zinc (Zn that has lost reactivity or has very low reactivity),” further

* Corresponding author.

E-mail address: yongliu@mail.buct.edu.cn (Y. Liu).

<https://doi.org/10.1016/j.cej.2025.159397>

Received 28 November 2024; Received in revised form 2 January 2025; Accepted 7 January 2025

Available online 10 January 2025

1385-8947/© 2025 Elsevier B.V. All rights are reserved, including those for text and data mining, AI training, and similar technologies.

contributes to capacity loss [20–22]. Side reactions such as hydrogen evolution reaction (HER) and surface passivation also exacerbate electrode degradation. The HER consumes the electrolyte [19,23], forming by-products like $\text{Zn}_4(\text{OH})_6\text{SO}_4 \cdot 5\text{H}_2\text{O}$, which hinder ion transport and increase interfacial resistance [24,25]. Finally, volume changes during cycling induce mechanical stress, accelerating electrode failure and reducing cycle life [15,26,27]. Research efforts have focused on three primary strategies to address these challenges: electrolyte engineering, separator designs, anode surface modification, and anode structural design.

Electrolyte engineering has shown promise in mitigating dendrite growth and HER by optimizing the Zn^{2+} solvation structure [28,29]. High-concentration electrolytes and hybrid systems enhance ionic conductivity and expand the electrochemical stability window [25]. Sambandam et al. demonstrated that low-concentration $\text{Zn}(\text{ClO}_4)_2$ electrolytes, with triethyl phosphate additives, improved structural stability and achieved higher reversible capacities [30]. Despite these advances, suppressing dendrites under high current densities remains challenging.

In addition to electrolytes, separators play a pivotal role in AZIBs' performance by facilitating ion transport, maintaining contact with electrodes, housing the electrolyte, and ensuring efficient battery operation [31,32]. Recent advancements have focused on modifying traditional glass fiber separators [33,34] and developing innovative cellulose-based [35,36], polyacrylonitrile-based [37,38], and graphene oxide-based membranes [39–41]. These separators leverage spatial restriction, electric field modulation, ion interaction forces, and desolvation effects to promote uniform Zn^{2+} migration and deposition, balance over-concentrated nucleation sites, and inhibit dendrite growth and side reactions [42]. Nevertheless, these separators' scalability and long-term stability remain constrained by the inherent limitations of materials and fabrication processes, hindering their broader market adoption.

Anode surface modification stabilizes zinc deposition by forming protective layers or modifying surface chemistry. Artificial protective layers like sulfonated polyaniline [43] and pectin gels [44] have been employed to construct solid electrolyte interphase (SEI) films. The ZnO (002) protective layer built on the Zn anode surface has been proven to significantly enhance zinc affinity and ion transport kinetics, mitigate side reactions, and promote uniform Zn deposition [45]. Bao et al. demonstrated that in situ formation of ZnF_2 SEI via N,N,N',N'-tetramethylchloromethaniminium hexafluorophosphate improved Zn^{2+} transport kinetics, promoting uniform deposition and dendrite suppression [46]. Similarly, recent studies have highlighted hybrid coatings of metal or covalent organic frameworks, which provide active sites for uniform zinc nucleation and reduce side reactions [47,48]. Zhang et al. reported a metal–organic framework –5W trilayer coating that accelerated ion transport and improved cycling stability [49]. Porous iCOF nanosheets with functional groups such as SO_3^- , C–O, and N–H [50], along with fluorinated zincophilic covalent organic frameworks containing sulfonic acid groups (COF-S-F), constructed on the Zn anode surface, have also been demonstrated to improve zinc deposition uniformity significantly [51]. However, interfacial impedance and mechanical stability persist, limiting long-term performance.

Anode structural and material design has shown significant potential in mitigating dendrite formation. Materials such as nickel-coated cotton [52], zinc-bismuth binary alloys [53], and MXenes and their derivatives have demonstrated positive effects in addressing this challenge [54]. Furthermore, developing three-dimensional (3D) architectures offers an additional robust and effective strategy to enhance zinc deposition uniformity and suppress dendrite growth [55–57]. These structures increase surface area, redistribute local current density, and provide abundant active sites for zinc deposition [56,58,59]. Techniques such as chemical etching, 3D printing, and electrospinning have been employed to fabricate such architectures [60–63]. Wang et al. developed a porous 3D Zn anode using an organic acid etching strategy, achieving uniform

deposition and enhanced cycling performance [64]. Similarly, Muhammad et al. utilized 3D printing to design PC/SiOC composite electrodes with tailored porosity, achieving superior cycling performance by controlling zinc nucleation [65]. 3D carbon networks grown in situ on zinc-based anodes fabricated through powder metallurgy techniques have also strongly inhibited zinc dendrite formation [66]. Furthermore, Lu et al. used electrospinning to develop a Sn-modified carbon fiber network, demonstrating high-capacity cycling stability [67]. These 3D architectures mitigate dendrite formation and address volumetric expansion issues, enhancing mechanical and electrochemical stability. Despite these advancements, integrating high conductivity, lipophilicity, and structural robustness into a single anode remains challenging.

Despite these advancements, current approaches face inherent limitations. Electrolyte engineering often fails to prevent dendrite formation under high current densities or prolonged cycling conditions. While influential in forming protective layers, surface modifications are frequently hampered by interfacial instability, increased impedance, and insufficient mechanical durability. Similarly, while 3D structures reduce localized current density and promote uniform Zn deposition, achieving the optimal combination of structural design and material properties remains challenging. Additionally, few studies have successfully integrated these strategies into a unified design to simultaneously address dendritic growth, HER suppression, and mechanical degradation.

This work proposes a novel zirconium oxide-doped carbon nanofiber (ZrO_2 -CF) 3D scaffold. This design combines carbon nanofibers' large surface area and high conductivity with the zincophilic and chemically stable properties of ZrO_2 . The ZrO_2 -CF scaffold addresses dendritic growth and HER suppression, delivering superior capacity retention, higher Coulombic efficiency, and extended cycling stability. These findings offer a scalable, high-performance solution for next-generation AZIBs.

2. Materials and Methods

2.1. Materials

Polyacrylonitrile (PAN, Mw = 150,000) was sourced from Tianjin Siense Biochemical Technology Co., Ltd. Zirconyl chloride ($\text{ZrOCl}_2 \cdot 8\text{H}_2\text{O}$, 99 %) was provided by Aladdin Biochemical Technology Co., Ltd. N, N-dimethylformamide (DMF, analytical grade), γ - MnO_2 (90 %), polyvinylidene fluoride (PVDF, Mw = 450,000), and N-methyl-2-pyrrolidone (NMP, analytical grade) were purchased from Macklin Reagent Co., Ltd., The electrolyte, a 1 M ZnSO_4 solution, was obtained from Aladdin Co., Ltd. In contrast, zinc foils were provided by Guangdong Canrd New Energy Technology Co., Ltd.

2.2. Preparation of 3-dimensional nanofiber scaffold

The preparation process for the 3-dimensional nanofiber scaffold is illustrated in Fig. 1, comprising electrospinning and subsequent thermal treatments. As shown in Fig. 1(A), the nanofiber mat was fabricated via electrospinning by dissolving PAN powder and $\text{ZrOCl}_2 \cdot 8\text{H}_2\text{O}$ in DMF (mass ratio of PAN: $\text{ZrOCl}_2 \cdot 8\text{H}_2\text{O}$: DMF = 0.3:0.3:2.2) (Fig. S1(A)). This mixture was stirred at room temperature for 10 h to obtain a homogeneous electrospinning solution. A 5 mL aliquot of this solution was then loaded into a 19G (0.67 mm inner diameter) needle for electrospinning under a 20 kV voltage. The fibers were collected on a rotating drum covered with silicone oil-coated paper, positioned 15 cm from the needle tip, and rotating at 400 rpm. To ensure a uniform fiber mat thickness, the solution was pumped at a rate of 0.8 mL h^{-1} , with the needle moving parallel to the drum at 50 mm min^{-1} .

The thermal treatment of the fiber mat, illustrated in Fig. 1(B), included drying, pre-oxidation, carbonization, and washing. The fiber mat was dried at $60 \text{ }^\circ\text{C}$ for 12 h to remove any residual solvent

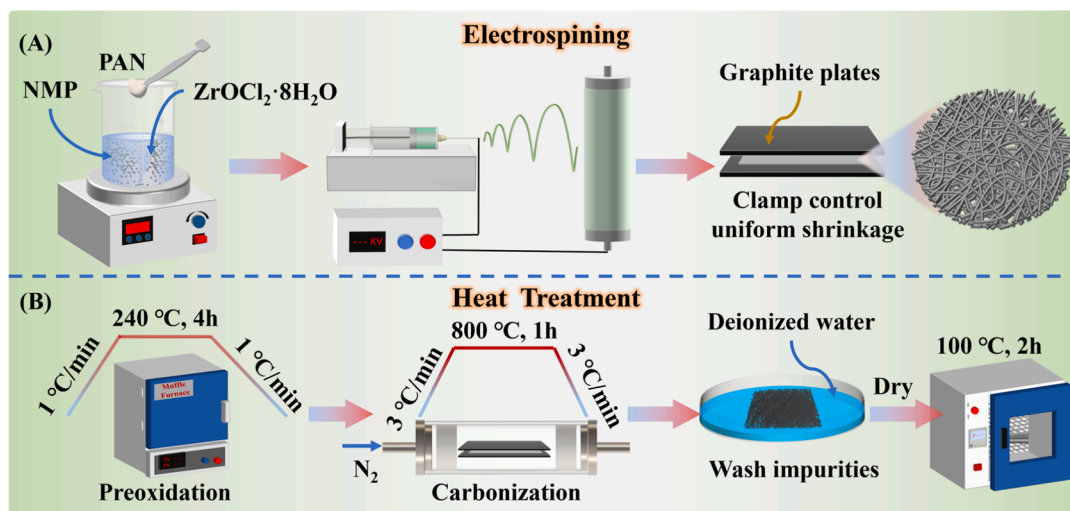


Fig. 1. The preparation process for the 3-dimensional nanofiber scaffold ((A) Preparation of nanofiber membrane by electrospinning, (B) Fiber membrane heat treatment process).

thoroughly. The dried mat was then carefully detached from the silicone oil paper and mounted between two 1-mm-thick graphite plates to ensure flatness. For pre-oxidation, the mat was heated in a muffle furnace under an air atmosphere at 240 °C for 4 h, with heating and cooling rates set to 1 °C min⁻¹. This pre-oxidation process promotes the cyclization of PAN chains and stabilizes the molecular structure (Fig. S1 (B)), thereby preventing melting or decomposition during subsequent high-temperature carbonization. The carbonization step was performed in a tube furnace under an argon atmosphere at 800 °C for 1 h, with heating and cooling rates maintained at 3 °C min⁻¹ (Fig. S1(C)). This step removed non-carbon elements, enhancing the resulting fibers' electrical conductivity and corrosion resistance while transforming ZrOCl₂·8H₂O into zirconia (ZrO₂) through dehydration and dechlorination. Finally, the carbonized fiber mat was washed with deionized water and dried in an oven at 100 °C for 2 h to yield the ZrO₂-doped carbon nanofiber (ZrO₂-CF) 3D scaffold with a thickness of approximately 90 μm (Fig. S1(D)).

For the preparation of the pure carbon fiber (CF) 3D scaffold, the process followed the same protocol as that for ZrO₂-CF scaffolds, with the only modification being the electrospinning solution. PAN was dissolved in DMF at a mass ratio of 0.3:2.2, omitting the zirconyl chloride additive.

2.3. Preparation of anode for AZIBs

The Zn@ZrO₂-CF 3D scaffold, serving as the anode for the AZIBs, was fabricated through an electrochemical deposition process. In this setup, the ZrO₂-CF scaffold acted as the cathode to facilitate Zn deposition, while a high-purity zinc foil served as the sacrificial anode. A 1 M ZnSO₄ aqueous solution was used as the electrolyte. Electroplating was conducted at a constant current density of 1 mA cm⁻² for 10 h, forming a uniform Zn layer across the scaffold surface, with a zinc deposition of 10 mAh cm⁻². Following deposition, the Zn-coated scaffold was thoroughly rinsed with deionized water and dried at room temperature.

For the preparation of the Zn@CF 3D scaffold, the procedure mirrored that of the Zn@ZrO₂-CF scaffold, with the sole modification being the substrate: pure carbon nanofiber scaffold was used as the deposition base for direct galvanization without zirconium oxide doping.

It is important to note that during the electroplating fabrication, the ZrO₂-CF or CF scaffold acts as the cathode to enable Zn deposition to prepare the Zn@ZrO₂-CF and Zn@CF anode. However, in the subsequent cell configuration, the Zn@ZrO₂-CF or Zn@CF 3D scaffold is the

anode, supporting Zn plating and stripping during battery operation.

2.4. Preparation of cells

All cells used in this study were CR2032 button cells with a 20 mm diameter. Electrodes were prepared by cutting the materials into 12 mm diameter circular disks, and a 19 mm diameter glass fiber separator was utilized. Stainless steel spacers and springs, each with a diameter of 15.8 mm, were employed. The electrolyte consisted of an aqueous solution of ZnSO₄.

For the MnO₂ cathode preparation, PVDF was dissolved in NMP to obtain a binder solution with a PVDF concentration of 0.025 g·mL⁻¹. Acetylene black and MnO₂ were added to this solution in a mass ratio of 7:2:1 and thoroughly mixed under magnetic stirring to form a homogeneous slurry. This slurry was evenly coated onto stainless steel foil and dried at 60 °C for 5 h to ensure adhesion. The average active material loading was confirmed to be approximately 1.6 mg cm⁻².

During battery assembly, the components were layered: negative shell, spacer, negative electrode, glass fiber separator, positive electrode, spacer, spring, and positive shell, as illustrated in Fig. S2(A). Notably, 4–5 drops of electrolyte were added after placing the separator to ensure complete saturation. After assembly, the cells were placed in a pressing mold and compressed at 60–70 MPa for 3 s, resulting in the completed aqueous zinc-ion button cells.

2.5. Morphological and structural characterization

To investigate the morphology and structure of the ZrO₂-doped carbon fiber membranes, 12 mm diameter circular samples were prepared. Samples were coated with a conductive layer and attached to double-sided conductive adhesive after liquid nitrogen fracture for cross-sectional imaging. The microstructure of the fibers was analyzed using a JEM-IT800 scanning electron microscope (SEM, JEOL, Japan) at magnifications of 10,000×, 50,000×, and 100,000 × .

For transmission electron microscopy (TEM) analysis, ZrO₂-CF membrane samples were finely ground, ultrasonicated in deionized water for 30 min, and dispersed onto copper grids. Using a JEM-2100F TEM (JEOL, Japan), the distribution of nanoparticles within individual fibers and the crystalline structure of surface particles were visualized.

Atomic force microscopy (AFM) analysis was conducted on 1 × 1 cm ZrO₂-CF samples affixed to mica substrates using a Bruker Dimension ICON AFM in Kelvin Probe Force Microscopy (KPFM) mode to assess surface roughness and potential distribution. A 1 × 1 μm scanning area

was selected, and the probe was advanced for surface scanning.

2.6. Phase composition characterization

Thermogravimetric analysis (TGA) of ZrO₂-CF membranes was conducted using a Hitachi 7200 thermogravimetric analyzer (Hitachi, Japan) under an air atmosphere. The temperature was raised from room temperature (25 °C) to 800 °C at a rate of 10 °C min⁻¹ to quantify carbon content and deduce ZrO₂ loading.

X-ray diffraction (XRD) analysis was conducted on ZrO₂-CF samples positioned on a recessed glass slide using an Empyrean XRD instrument (Malvern Panalytical, Netherlands) with a copper target ($\lambda = 0.154$ nm, K α). Scans were performed over a 2θ range of 10° to 90° at a rate of 5°/min to evaluate sample crystallinity and lattice plane indices.

To determine the surface elemental composition, 1 × 1 cm square ZrO₂-CF samples were adhered to aluminum foil using conductive glue and analyzed by X-ray photoelectron spectroscopy (XPS) on a Thermo Scientific ESCALAB Xi + system (Thermo Fisher Scientific, USA).

2.7. Electrochemical performance

2.7.1. Symmetric cell test

For the symmetric cell test, bare Zn foil and Zn-electroplated 3D scaffolds (Zn@ZrO₂-CF and Zn@CF, with a Zn deposition of 10 mAh cm⁻²) were used as the working anodes, paired against Zn foil as the counter electrode. The electrolyte was a 1 M ZnSO₄ aqueous solution, and glass fiber (Whatman, UK) was the separator. Cells were assembled in CR2032 coin cells and subjected to galvanostatic cycling at current densities of 10 and 20 mA cm⁻², with a charge–discharge capacity of 1 mAh cm⁻² to evaluate the cycling stability of Zn@ZrO₂-CF and Zn@CF.

2.7.2. Half cell test

ZrO₂-CF, CF, and bare Zn were employed as working anodes in the half-cell configuration, paired with high-purity Zn foil as the counter electrode. A 1 M ZnSO₄ aqueous solution was used as the electrolyte. During Zn stripping, a cut-off potential of 0.5 V was set, and the galvanostatic charge–discharge tests were conducted at current densities of 5 mA cm⁻² and 10 mA cm⁻², with discharge capacities of 1.25 mAh cm⁻² and 2.5 mAh cm⁻², respectively. These tests assessed the Coulombic efficiency and cycling stability of the ZrO₂-CF and CF 3D scaffold anodes, ensuring reliable and reproducible results.

For linear sweep voltammetry (LSV), the potential range was set from -0.8 V to 0.2 V at a scan rate of 2 mV s⁻¹, with a 1 M Na₂SO₄ aqueous solution as the electrolyte to isolate any interference from electrode reactions. The LSV tests, conducted using a CS 310 M electrochemical workstation, evaluated the influence of the ZrO₂-CF and CF working anodes on the HER.

2.7.3. Full cell test

To comprehensively evaluate the cycling stability of the prepared Zn@ZrO₂-CF anode, total cells were assembled using Zn@ZrO₂-CF with a zinc deposition of 10 mAh cm⁻² and bare zinc as anodes, paired with MnO₂ as the cathode material (active mass loading: 1.4 mg cm⁻²). The electrolyte comprised a 1 M ZnSO₄ and 0.1 M MnSO₄ aqueous solution, where MnSO₄ was included to mitigate MnO₂ dissolution by maintaining Mn²⁺ ions in equilibrium. Cell assembly and testing were conducted on a Neware CT 4008 T system, starting with 20 pre-cycling steps at a current density of 0.5 mA cm⁻² within a potential range of 0.8–1.8 V to activate the electrodes. Following activation, cycling stability was evaluated under constant current conditions, and cell capacity was assessed across varying current densities. Cyclic voltammetry (CV) curves of the entire cells were obtained using a CS 310 M electrochemical workstation with a controlled voltage scan rate of 0.1 mV s⁻¹.

2.8. Simulation method

2.8.1. Finite element method

Finite element simulations were conducted using COMSOL Multiphysics 6.0 (COMSOL Inc., Sweden) to develop detailed surface models for zinc plates and a comprehensive 3D scaffold structure. These simulations leveraged the electrostatics, secondary current distribution, and dilute species transport modules to evaluate electric field distribution, current density, and plating thickness across different model configurations. These analyses aimed to investigate the influence of the 3D scaffold structure on electrode reactions, particularly regarding electric field uniformity and current distribution.

In the zinc plate model, the zinc discs (diameter 12 mm, height 10 mm) featured randomly distributed hemispherical protrusions (radius 0.5 mm) to replicate natural surface morphology (Fig. S2(B)). The 3D scaffold model included fibers with a diameter of 1 mm and a spacing of 3 mm within an electrolyte region defined as a 20 mm cube (Fig. S2(C)). Key parameters included an exchange current density of 19.68 mA cm⁻² for the electrode, an electrolyte conductivity of 5 S m⁻¹ for ZnSO₄, and a 10 mA cm⁻² current density in the electrolyte. The working electrode's surface potential was fixed at 0.5 V, with the total system potential set to 0 V, and simulations were conducted at 293.15 K.

Steady-state simulations provided spatially resolved electric field and local current density distributions, while transient simulations assessed the temporal evolution of plating thickness. The main governing equations are listed below, while other computational procedures followed the standardized algorithms embedded within COMSOL Multiphysics 6.0.

The electric field intensity E and electric potential ϕ were represented by Poisson's equation:

$$E = -\nabla\phi = -\nabla\varphi \quad (1)$$

where E indicates the electric field strength, mass conservation for species i within the electrolyte was represented by:

$$\frac{\partial C_i}{\partial t} + \nabla J_i = R_i \quad (2)$$

where J_i is the flux of species i , C_i is its concentration, and R_i the reaction rate (set to zero under non-reactive conditions). The Nernst-Planck equation governed ion flux, encompassing diffusion and migration effects [68]:

$$J_i = -D_i \nabla C_i - z_i u_{m,i} F C_i \nabla \phi \quad (3)$$

where D_i is the diffusion coefficient, z_i is the ion charge, $u_{m,i}$ is the mobility, F is the Faraday constant, and $\nabla \phi$ is the potential gradient. The convection term was omitted, assuming a stationary electrolyte. The local current density (*iloc. expr*) was calculated using the Butler-Volmer equation to relate current density to overpotential [69]:

$$i_{loc, expr} = i_0 \left(C_R \exp\left(\frac{\alpha_a F \eta}{RT}\right) - C_O \exp\left(\frac{-\alpha_c F \eta}{RT}\right) \right) \quad (4)$$

where i_0 is the exchange current density, C_R and C_O are the concentrations of the reduced and oxidized species, α_a and α_c are the anodic and cathodic transfer coefficients, η is the overpotential, R is the gas constant, and T is the absolute temperature.

This modeling approach, structured with clear parameters and boundary conditions, effectively captures the spatial and temporal behaviors of the 3D scaffold, elucidating its role in enhancing field uniformity and optimizing current density distributions for improved plating stability.

2.8.2. Density functional theory simulation

To evaluate the affinity between ZrO₂ and Zn, first-principles calculations based on quantum mechanics were performed using the

CASTEP module in the Materials Studio software (Accelrys Inc., USA). These calculations employed density functional theory (DFT) to determine the binding energy of Zn atoms on various substrate surfaces. The Perdew-Burke-Ernzerhof (PBE) generalized gradient approximation (GGA) functional was utilized for total energy calculations, with ultrasoft pseudopotentials applied to model core electrons [70,71].

Crystal plane models (101), (112), and (211) were generated by slicing and expanding the optimized crystal structures into a $2 \times 3 \times 1$ supercell. For each surface, the optimal Zn adsorption site was identified as the minimum energy point using the Absorption Locator module in Materials Studio. An energy cut-off of 571.4 eV was set, which is commonly sufficient for accuracy with ultrasoft pseudopotentials, ensuring a balance between computational efficiency and accuracy. The vacuum layer thickness was maintained at 15 Å to prevent spurious interactions between periodic images. The Brillouin zone was sampled using a Monkhorst-Pack grid, with a $3 \times 3 \times 1$ k-point mesh applied to enhance the sampling accuracy, particularly for surfaces exhibiting significant electronic behavior. Binding energies (E_{bound}) of Zn atoms on the graphite fiber and ZrO_2 crystal surfaces were calculated using Eq. (5):

$$E_{\text{bound}} = E_{\text{total}} - E_{\text{sub}} - E_{\text{Zn}} \quad (5)$$

where E_{bound} is the binding energy of Zn to the substrate, E_{total} represents the total energy of the combined Zn-substrate model, E_{sub} is the energy of the substrate (graphite or ZrO_2), and E_{Zn} denotes the power of an isolated Zn atom.

To ensure computational reliability, convergence criteria were established with an energy tolerance of 1×10^{-5} eV and a force

tolerance of $0.01 \text{ eV } \text{Å}^{-1}$. This simulation framework provides a robust understanding of the interaction energy and affinity between Zn and ZrO_2 surfaces, thereby offering insights into the potential anchoring effect of ZrO_2 on Zn atoms. All computational procedures employed well-established algorithms within the CASTEP package, ensuring reliability and reproducibility.

3. Results and discussion

3.1. Morphology and structural characteristics of the 3D scaffold

The morphology of the zirconium oxide-doped carbon nanofiber scaffold, designed as an anode for aqueous Zinc-ion batteries, demonstrates a complex porous fiber network with tightly interfaced but unevenly spaced fibers (Fig. 2(A and B)). Cross-sectional images display a disordered, multilayered arrangement, where fibers are unevenly spaced but structurally cohesive (Fig. 2(C and D)), confirming the formation of a robust 3D scaffold. Energy-dispersive X-ray mapping (Fig. 2 (E and F)) confirms the uniform distribution of zirconium oxide across both the fiber surface and interior, with the zirconium content around 40%, consistent with thermogravimetric analysis (Fig. S3(A)). AFM and KPFM data further illustrate the differences between the zirconium oxide-doped 3D scaffold and pure Zn anodes (Fig. 2(G and H)). The zirconium oxide-doped 3D scaffold shows a smoother surface (peak-to-valley height: -52.7 nm to $+56.2 \text{ nm}$) and more uniform surface potential (549.9 mV to 625.6 mV) compared to the rougher pure Zn surface (peak-to-valley height: -146.1 nm to $+107.3 \text{ nm}$; potential: 970.8 mV to 1300.0 mV) (Fig. S3(B)). The smoother, electrically stable scaffold is attributed to the high carbonization degree and material-specific

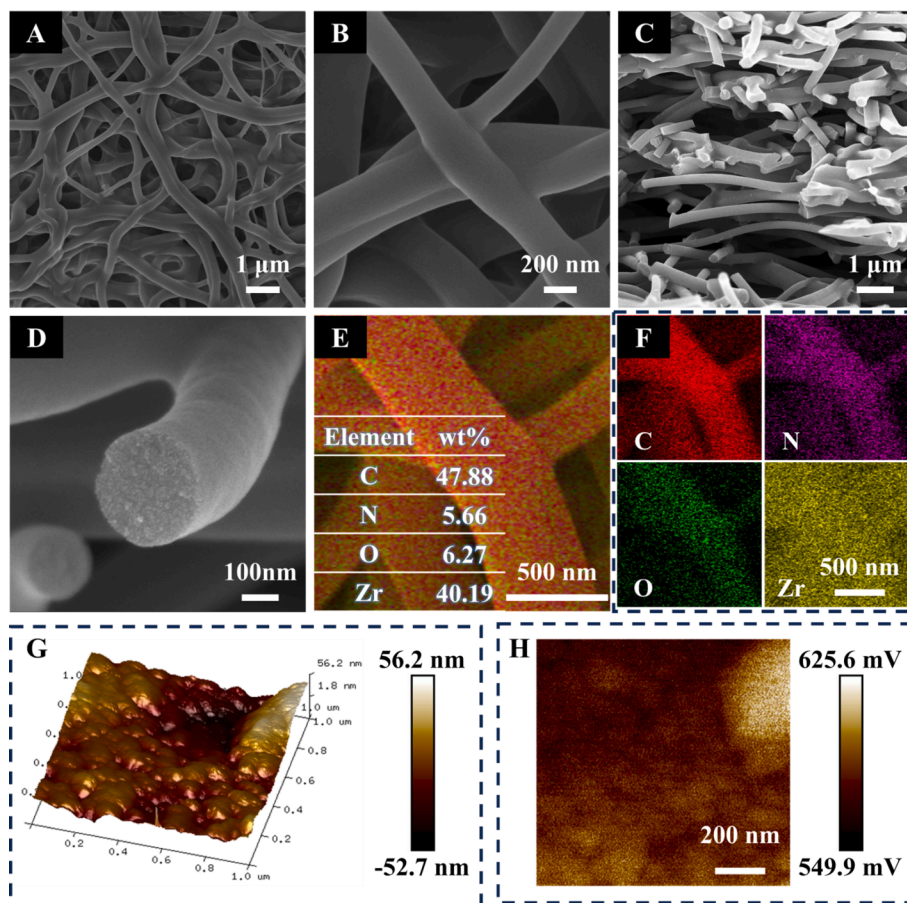


Fig. 2. Microstructural analysis of the 3D scaffold: (A, B) Top-view morphology at different magnifications; (C, D) Cross-sectional morphology at varying magnifications; (E, F) Surface elemental mapping, illustrating the spatial distribution of critical elements within the scaffold structure; (G, H) Surface roughness and potential.

properties that improve zinc deposition uniformity and mitigate dendrite formation.

TEM images (Fig. S3(C)) highlight the uniform distribution of granular particles on the fiber surface, distinguishing between carbonaceous and non-carbon crystalline regions to further elucidate the microstructure and composition. Elemental mapping confirms the presence of C, N, O, and Zr, suggesting successful doping of zirconium oxides. HRTEM analysis (Fig. 3(A)) identifies lattice fringes corresponding to the (101) and (112) planes of ZrO_2 [72], substantiating that zirconium exists in the form of ZrO_2 .

XRD patterns (Fig. 3(B)) further validate these observations. The undoped scaffold exhibits a sharp diffraction peak corresponding to the (002) plane of graphitic carbon, indicating complete carbonization of PAN. In contrast, the ZrO_2 -doped scaffold shows additional diffraction peaks at $2\theta = 30^\circ, 34^\circ, 50^\circ,$ and 60° , assigned to the (101), (110), (112), and (211) planes of ZrO_2 [73]. This confirms the uniform incorporation of ZrO_2 within the scaffold's structure. FTIR spectra (Fig. S3(D)) reinforce these findings, revealing characteristic Zr—O vibrations and potential C—O—Zr, N—Zr—O bridge bonds, which may enhance mechanical stability and mitigate electrode deformation during cycling.

XPS analysis (Fig. S3(E)) supports the elemental composition, showing only C, N, O, and Zr in the ZrO_2 -doped scaffold [74]. High-resolution C 1s spectra (Fig. 3(C)) indicate that carbon predominantly exists in C—C, C—N, and C—O configurations, contributing to the scaffold's excellent conductivity. The N 1s spectrum (Fig. 3(D)) reveals the presence of pyridinic N, pyrrolic N, and N—Zr—O bridge bonds, which play critical roles in enhancing the anode's electrochemical performance. Pyridinic N provides zincophilic sites for uniform Zn deposition and mitigates HER by reducing H adsorption. Due to its unique electronic structure, Pyrrolic N forms N—H bonds that increase the energy barrier for HER, further suppressing this side reaction; additionally, the presence of N—Zr—O bridge bonds enhances the adsorption capacity for Zn^{2+} ions, offering supplementary anchoring points to

promote uniform Zn deposition. In the O 1s narrow scan (Fig. 3(E)), apart from C—O and Zr—O bonds, a peak near 533 eV suggests the presence of C—O—Zr bonds, further corroborated by FTIR analysis.

Furthermore, there is a slight leftward shift in the binding energy of Zr—O to 530.18 eV, deviating by approximately 0.1–0.3 eV. This shift indicates that the N—Zr—O bridge bonds are likely overlapped by Zr—O bonds. These bonds likely improve the scaffold's mechanical properties, ensuring structural stability under cycling conditions. They also enhance the uniformity of the electric field distribution, promoting even Zn deposition and reducing the risk of dendrite formation. Finally, Zr 3d XPS spectra (Fig. 3(F)) show two peaks at 182.1 eV and 184.5 eV, corresponding to the $3d_{5/2}$ and $3d_{3/2}$ orbitals of ZrO_2 . Notably, the $3d_{5/2}$ binding energy shifts slightly to the left by approximately 0.2 eV, nearing 182.0 eV. This shift provides further evidence for C—O—Zr and N—Zr—O bridge bonds [75,76]. Additionally, it confirms the high purity of ZrO_2 after the carbonization process, underscoring its structural and chemical integrity.

So, the zirconium oxide-doped 3D scaffold (Abbreviated as ZrO_2 -CF scaffold or ZrO_2 -CF), produced by electrospinning and thermal treatment, demonstrates a distinctive 3D network structure, uniform ZrO_2 dispersion, and a high degree of carbonization. The scaffold's C—C, C—N, C—O bonds, and N—Zr—O, C—O—Zr bridging bonds contribute to its mechanical strength, conductivity, and favorable surface properties, and smooth, conductive surface structure, aids in suppressing HER and promotes uniform Zn deposition, supporting long-term cycling stability and improved Coulombic efficiency in aqueous zinc-ion batteries.

3.2. Deposition behavior of Zn on anode 3D scaffold

The Zn deposition behavior on different 3D scaffolds was systematically evaluated to understand the impact of ZrO_2 doping on mitigating dendrite formation. Fig. 5 demonstrates the Zn deposition process on pure Zn and ZrO_2 -CF anodes under a high current density of 10 mA cm^{-2}

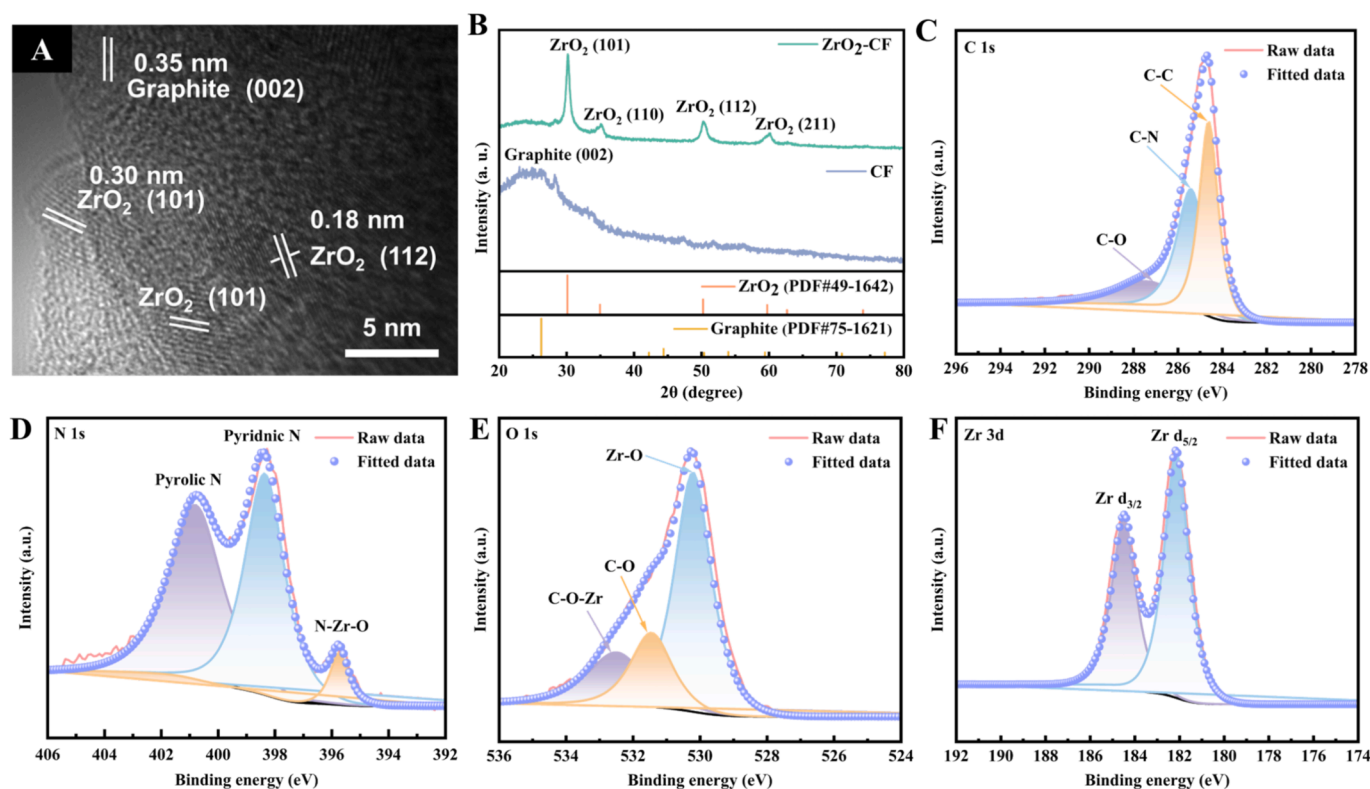


Fig. 3. Characterization of the 3D scaffold: (A) HRTEM image; (B) XRD pattern; and XPS high-resolution spectra for (C) carbon (C 1s), (D) nitrogen (N 1s), (E) oxygen (O 1s), and (F) zirconium (Zr 3d).

with a 1 mA h cm^{-2} discharge capacity. After just 1 h of cycling, the pure Zn anode exhibited significant surface roughness, indicating the onset of uneven Zn deposition. Over time, these surface irregularities evolved into prominent protrusions, serving as nucleation sites for dendrite growth. By the 10th hour, distinct dendritic structures were observed on the Zn anode (Fig. 4(A)), highlighting the risk of short circuits and active material loss due to dendrite formation. In contrast, the ZrO_2 -CF 3D scaffold maintained a smooth surface after 10 h of cycling, with no visible dendritic growth or rough platforms (Fig. 4(B)); this demonstrates the scaffold's effectiveness in suppressing dendrite formation, thereby enhancing the cycling stability of the anode.

Further investigations were conducted to evaluate the deposition behavior under varying current densities. Fig. 5 presents the surface morphology of Zn@CF and $\text{Zn@ZrO}_2\text{-CF}$ scaffolds after 100 deposition cycles at current densities of 1, 5, and 10 mA cm^{-2} . For the CF scaffold, at a low current density of 1 mA cm^{-2} , Zn exhibited non-uniform and random deposition on the fiber surfaces, with some regions showing vertical growth (Fig. 5(A1 and A2)). As the current density increased to 5 mA cm^{-2} , Zn filled the inter-fiber voids, with most fiber surfaces fully encapsulated (Fig. 5(B1 and B2)). Although no significant dendrites were observed, the fibers were heavily coated, obscuring their original structure. At 10 mA cm^{-2} , Zn completely replaced the fiber structure, forming a layered Zn morphology with rough and uneven surfaces (Fig. 5(C1 and C2)). These rough surfaces could act as new dendritic growth platforms, leading to potential active material loss and reduced battery performance.

In stark contrast, the ZrO_2 -CF 3D scaffold exhibited significantly improved deposition behavior. At 1 mA cm^{-2} , Zn formed a thin, uniform layer along the fibers, preserving the scaffold's porous structure (Fig. 5(D1 and D2)). As the current density increased to 5 mA cm^{-2} , Zn continued to deposit uniformly along the fiber surfaces without filling the inter-fiber voids, maintaining a clear fiber morphology (Fig. 5(E1 and E2)). Even at a high current density of 10 mA cm^{-2} , the fiber structure remained intact, with Zn growing uniformly along the fibers and no visible dendrite formation (Fig. 5(F1 and F2)). This improved performance is attributed to the C—O—Zr bridge bonds identified in XPS and FTIR analyses, which enhance the scaffold's mechanical stability and promote homogeneous Zn nucleation and growth.

Overall, the 3D architecture of both CF and ZrO_2 -CF scaffolds provides ample space for Zn deposition, reducing the probability of dendrite formation. However, the ZrO_2 -CF scaffold outperforms the undoped CF scaffold, particularly at higher current densities. The well-preserved fiber structure and uniform Zn deposition observed in the ZrO_2 -CF scaffold highlight its potential to enhance the performance and safety of

aqueous Zn-ion batteries. By facilitating even Zn growth and suppressing dendrite formation, the ZrO_2 -CF scaffold addresses critical challenges associated with Zn anodes, ensuring improved cycling stability and Coulombic efficiency.

3.3. Mechanism of action of ZrO_2 -CF 3D scaffold

During the electrodeposition process, the voltage profiles of both ZrO_2 -CF and CF 3D scaffolds exhibit an initial sharp drop, gradually increasing until stabilizing at a plateau potential (Fig. 6(A)). This behavior corresponds to the nucleation of zinc metal. Notably, the ZrO_2 -CF scaffold shows a significantly lower nucleation overpotential (27 mV) compared to CF (50 mV), indicating that ZrO_2 doping effectively reduces the nucleation potential of Zn on the 3D scaffold. This enhancement accelerates electrode reaction kinetics, promoting more efficient Zn deposition.

Further supporting this, DFT calculations reveal that the binding energies of Zn atoms on ZrO_2 's primary crystal planes—(1 0 1), (1 1 2), and (2 1 1)—are -0.92 eV , -0.35 eV , and -3.34 eV , respectively, which are substantially higher than the -0.025 eV observed for the graphite (0 0 2) plane (Fig. 6(B)). These findings underscore the critical role of ZrO_2 in providing highly active Zn-affinity sites. The firm "anchoring effect" induced by ZrO_2 facilitates lower nucleation potentials and directs Zn deposition along the scaffold surface, resulting in more uniform growth. Combining these theoretical insights with XPS analysis, it is evident that the enhanced performance of ZrO_2 -CF can be attributed to the formation of C—O—Zr bridge bonds and the inherent Zn-philic properties of ZrO_2 . These features synergistically lower the energy barrier for Zn nucleation and promote homogeneous deposition, significantly improving the anode's electrochemical stability and cycling performance.

The COMSOL Multiphysics simulation results indicate that defects and surface irregularities introduced during the processing or cutting of the pure Zn anode act as electric field concentration points. These areas exhibit significant field intensification near protrusions (Fig. 6(C)), leading to non-uniform Zn deposition and an increased likelihood of dendrite formation. In contrast, the ZrO_2 -CF scaffold demonstrates a more uniform electric field distribution (Fig. 6(D)), consistent with the AFM analysis. Furthermore, comparative studies of surface current density and Zn deposition thickness at the initial deposition stage and after 1800 s (Fig. S4), 3600 s reveal stark differences between the two anodes. On the Zn foil, regions with concentrated electric fields exhibit higher local current densities, resulting in disproportionate Zn deposition. This uneven deposition accelerates dendrite growth and

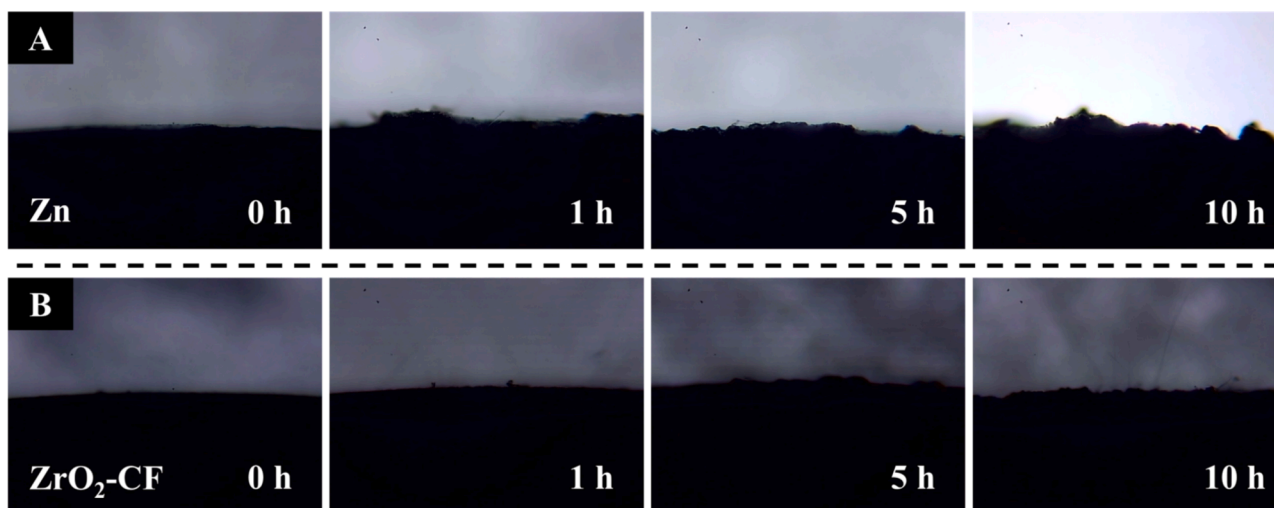


Fig. 4. Optical microscopy images illustrating zinc deposition behavior on zinc foil (A) and ZrO_2 -CF 3D scaffold (B) anodes over varying electrodeposition cycles.

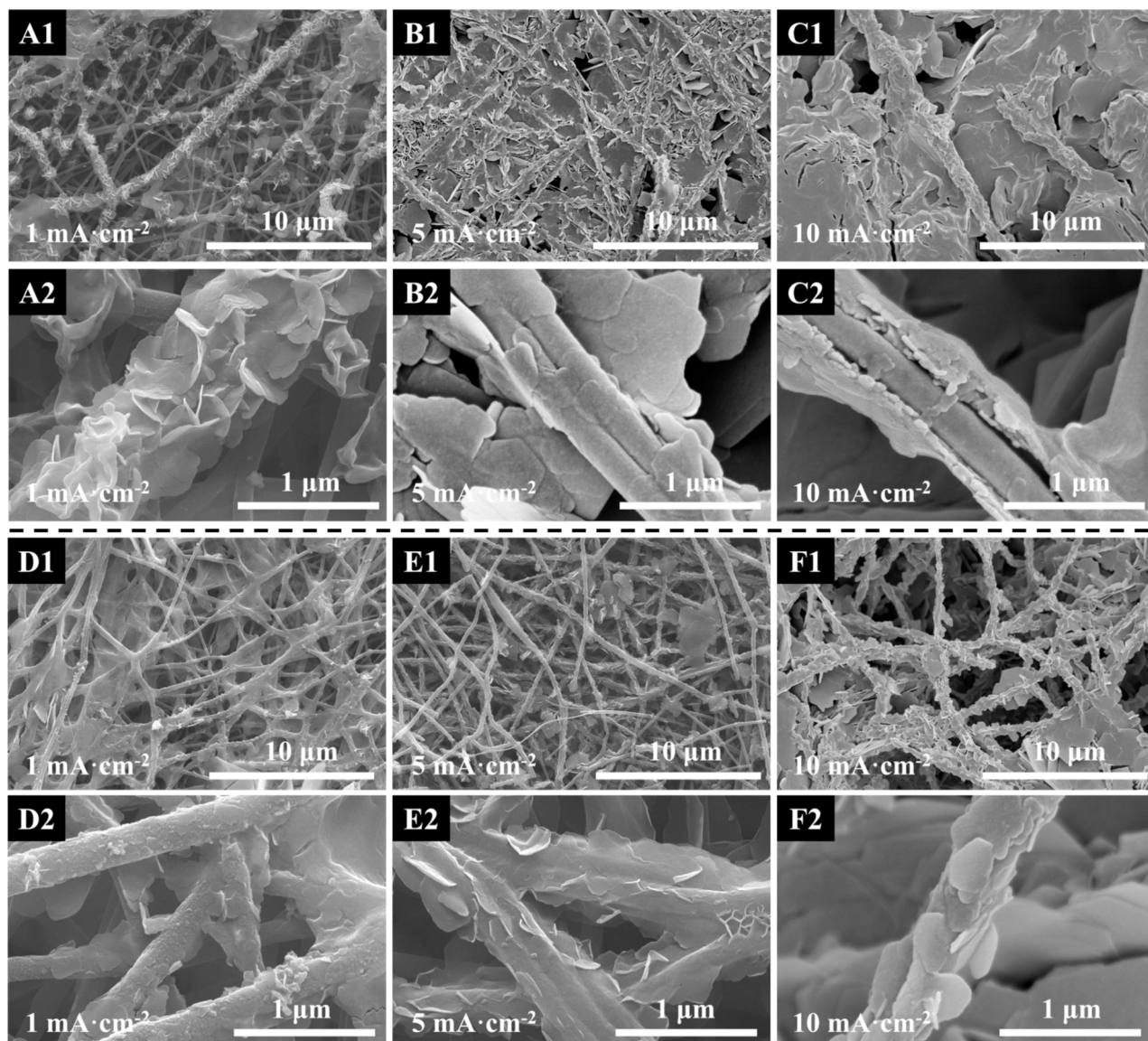


Fig. 5. Surface morphology of CF and ZrO₂-CF 3D scaffolds after 100 electrodeposition cycles at varying current densities. Panels (A1, A2), (B1, B2), and (C1, C2) show the CF 3D scaffold at current densities of 1 mA cm⁻², 5 mA cm⁻², and 10 mA cm⁻², respectively. Panels (D1, D2), (E1, E2), and (F1, F2) display the ZrO₂-CF 3D scaffold under the same conditions.

exacerbates concentration polarization, creating a feedback loop of deteriorating electrode performance (Fig. 6(E and F)).

Conversely, the ZrO₂-CF scaffold benefits from its 3D architecture, which offers a high surface area and extensive electron transport pathways; this “spatial effect” promotes uniform electric field and current density distribution, significantly reducing concentration polarization and dendrite formation risk (Fig. 6(G and H)). These improvements contribute to enhanced battery lifespan and safety.

Moreover, the Nyquist plots (Fig. 7(A)) demonstrate that ZrO₂-CF and CF scaffolds exhibit lower charge transfer resistance than pure Zn anode. Notably, ZrO₂-CF shows the lowest charge transfer resistance, attributed to the synergistic effects of C—O—Zr bridge bonds and ZrO₂'s Zn-philic properties. These features facilitate faster electron transfer and ion migration, promoting uniform Zn deposition and mitigating dendrite growth.

Similarly, full-cell cyclic voltammetry results confirm the reduced polarization effect. The Zn@ZrO₂-CF // MnO₂ cell exhibits a narrower oxidation–reduction potential gap (140 mV) compared to the Zn // MnO₂ cell (211 mV), with a reduction of approximately 71 mV (Fig. 7

(B)). This improvement underscores the role of the ZrO₂-CF scaffold's unique 3D network structure, C—O—Zr bridge bonds, and Zn-philic properties in minimizing polarization effects and enhancing overall battery performance.

The HER at the Zn anode is a critical factor affecting the cycling stability of aqueous Zn-ion batteries, as it contributes to parasitic side reactions and reduces Coulombic efficiency. Fig. 7(C) shows the LSV curves for ZrO₂-CF and CF 3D scaffolds, which reflect their HER behavior. At a current density of 5 mA cm⁻², the ZrO₂-CF scaffold exhibits a lower HER overpotential (−0.75 V) compared to CF (−0.67 V), demonstrating superior HER suppression. This enhancement can be attributed to the Zn-philic sites provided by ZrO₂ and the high electronegativity of pyrrolic N, which hinder hydrogen adsorption and evolution, as corroborated by the structural analysis of the 3D scaffold.

These results align with the scaffold's “spatial effect” and “anchoring effect.” The 3D architecture of ZrO₂-CF provides abundant deposition sites and facilitates uniform Zn nucleation and growth, mitigating local current density spikes and dendrite formation. Meanwhile, the presence of Zn-philic ZrO₂ sites, C—O—Zr bridge bonds, and nitrogen-based

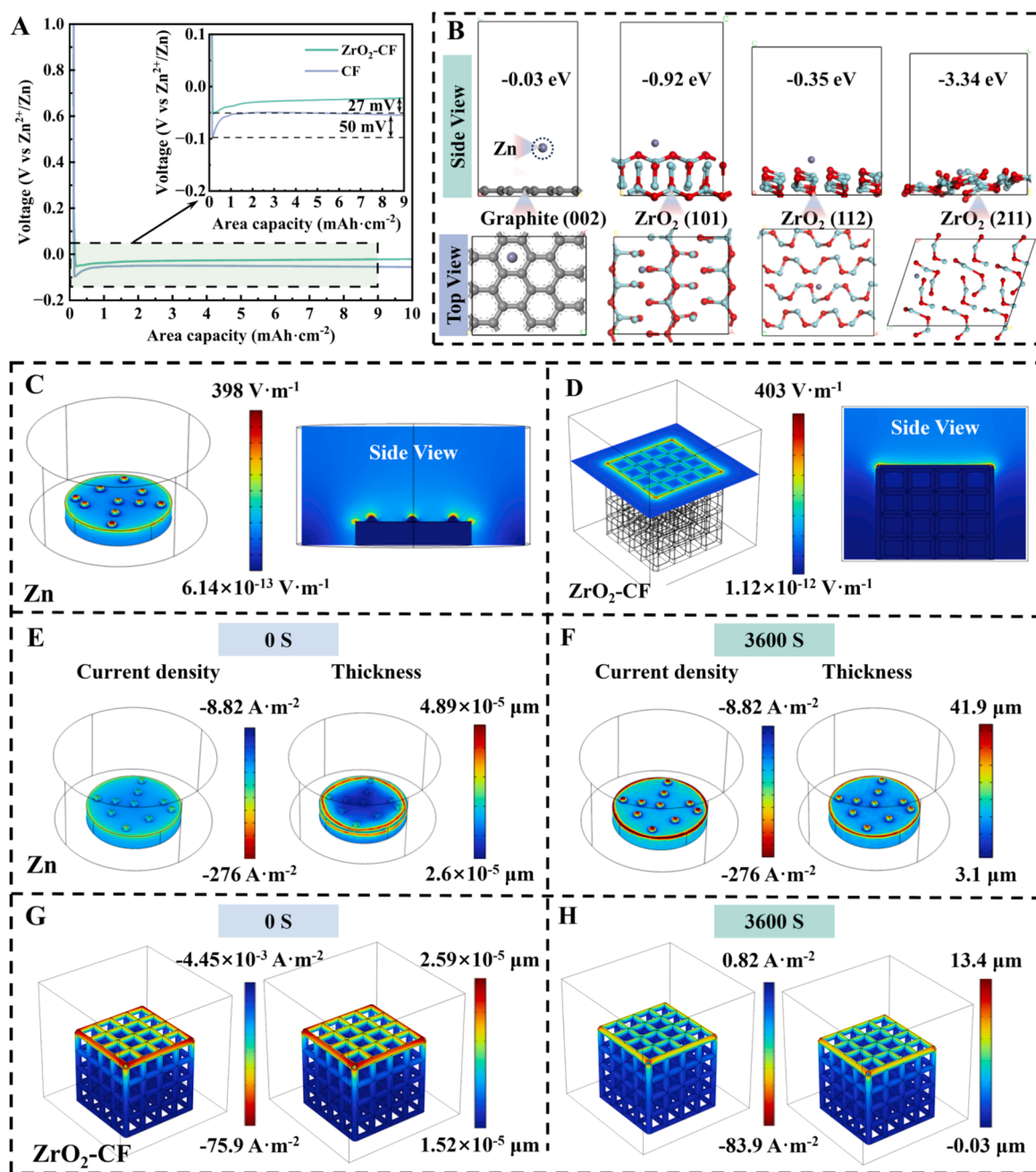


Fig. 6. (A) Voltage profiles of Zn electrodeposition on ZnO₂-CF and CF scaffolds under identical cycling conditions. (B) Adsorption models of Zn atoms on the graphite (002) plane and ZnO₂ crystal planes: (101), (112), and (211). (C, D) Electric field distribution on Zn foil and 3D scaffold surfaces, respectively. (E, F) Surface current density and Zn deposition thickness distribution on Zn foil at the initial deposition stage and after 3600 s. (G, H) Surface current density and Zn deposition thickness distribution on the 3D scaffold at the initial deposition stage and after 3600 s.

functional groups ensures a uniform electric field and current density distribution, improving electron transfer efficiency and HER resistance (Fig. 7(D)). Under the combined influence of these effects, the ZnO₂-CF scaffold significantly reduces the occurrence of dendrites and alleviates concentration and ohmic polarization. This dual-action mechanism enhances the cycling stability and safety of aqueous Zn-ion batteries, further validating the effectiveness of ZnO₂-CF as an advanced anode material.

3.4. Performance of Zn@ZnO₂-CF anode

To evaluate the cycling stability of Zn@ZnO₂-CF, Zn@CF, and Zn foil anodes, symmetrical cells were assembled for galvanostatic charge/

discharge tests. At current densities of 10 mA cm⁻² and 20 mA cm⁻², the Zn foil-based cells showed a sudden drop in overpotential after ~25 h, caused by short circuits due to dendrite penetration through the separator. In contrast, the Zn@CF anode demonstrated better initial stability but showed significant overpotential fluctuations after 60–100 cycles. This instability is likely due to a lack of Zn-affinitive sites and side reactions, leading to active Zn loss and eventual depletion of Zn deposits on the scaffold surface.

The Zn@ZnO₂-CF anode exhibited superior stability, maintaining performance for over 200 h (1,000 cycles) with lower overpotentials under various current densities (1, 3, 5, 10, and 20 mA cm⁻²). The overpotentials were approximately 23, 45, 59, 85, and 136 mV, respectively, as shown in Fig. 8(A and B). These values were significantly

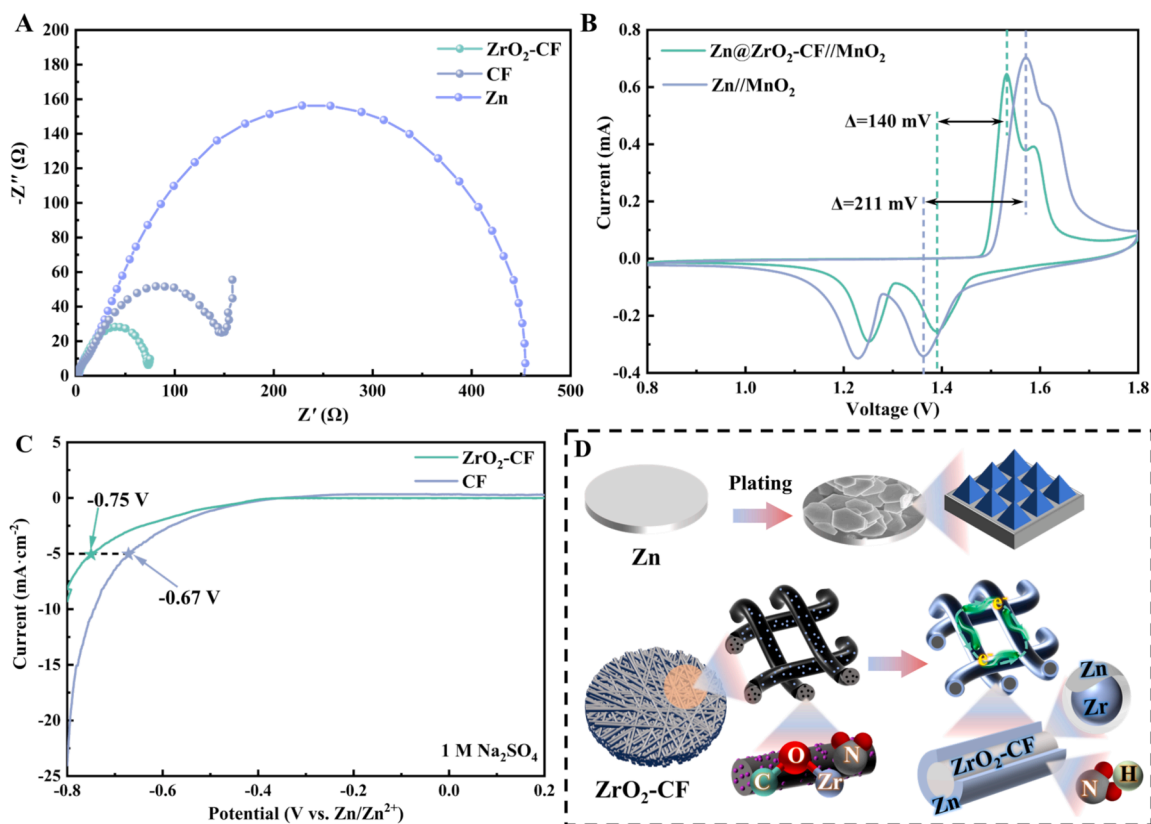


Fig. 7. (A) Electrochemical impedance spectroscopy (EIS) curves of $\text{ZrO}_2\text{-CF}$, CF, and Zn in half cells. (B) CV curves of $\text{Zn@ZrO}_2\text{-CF//MnO}_2$ and Zn//MnO_2 in full cells. (C) LSV curves of $\text{ZrO}_2\text{-CF}$ and CF 3D scaffolds in half cells. (D) Schematic illustration of the “spatial effect” and “anchoring effect” mechanisms of the $\text{ZrO}_2\text{-CF}$ 3D scaffold.

lower than those of Zn@CF (Fig. S5(A)) and Zn foil (Fig. S5(B)), indicating faster Zn^{2+} transport and improved interfacial stability. These results confirm the combined effects of the porous 3D structure (“spatial effect”) and ZrO_2 doping (“anchoring effect”) in enhancing cycling stability.

Coulombic efficiency tests further highlight the advantages of the $\text{Zn@ZrO}_2\text{-CF}$ anode. CF anodes without ZrO_2 doping in half-cell configurations showed unstable voltage profiles and large Coulombic efficiency fluctuations after just 40 cycles. The Coulombic efficiency dropped to nearly zero after 60–70 cycles (Fig. 8(C and D)). This was caused by excessive dendrite growth, leading to the formation of “dead Zn” and detachment of active material. In contrast, the $\text{Zn@ZrO}_2\text{-CF}$ anode achieved stable cycling with average Coulombic efficiency of 96.53 % and 98.61 % under current densities of 5 mA cm^{-2} and 10 mA cm^{-2} , respectively, over 100 cycles (Fig. S6). These results demonstrate that the ZrO_2 “anchoring effect” effectively suppresses dendrite growth and maintains high Coulombic efficiency during cycling.

To evaluate the performance of the composite anode in practical applications, a full cell was assembled using $\text{Zn@ZrO}_2\text{-CF}$ as the anode and MnO_2 as the cathode. During cyclic voltammetry tests, the cell exhibited highly overlapping curves over four cycles (Fig. 9(A)), indicating excellent reversibility of the $\text{Zn@ZrO}_2\text{-CF}$ anode. At both high ($1,000 \text{ mA g}^{-1}$) (Fig. 9(B)) and low (200 mA g^{-1}) (Fig. 9(C)) current densities, the $\text{Zn@ZrO}_2\text{-CF//MnO}_2$ cell showed higher initial discharge capacities (75 mAh g^{-1} vs. 64 mAh g^{-1} and 124.3 mAh g^{-1} vs. 114.8 mAh g^{-1} , respectively) and more stable Coulombic efficiencies compared to the Zn//MnO_2 cell. After 1,000 cycles at $1,000 \text{ mA g}^{-1}$, the $\text{Zn@ZrO}_2\text{-CF//MnO}_2$ cell retained 47 % of its initial capacity, significantly outperforming the Zn//MnO_2 cell, which retained only 26.5 %. At 200 mA g^{-1} , the $\text{Zn@ZrO}_2\text{-CF//MnO}_2$ cell retained 76.8 % of its capacity after 100 cycles, compared to 61 % for the Zn//MnO_2 cell (Fig. 9

(C)). Moreover, the $\text{Zn@ZrO}_2\text{-CF//MnO}_2$ cell demonstrated superior rate performance, as evidenced by more stable and reversible capacity retention than the Zn//MnO_2 cell (Fig. 9(D) and Fig. S7(A)).

So, the 3D porous structure of the $\text{ZrO}_2\text{-CF}$ scaffold reduces dendrite formation and suppresses side reactions by leveraging its “spatial effect” and “anchoring effect.” This design minimizes the formation of “dead Zn,” enhances Zn plating/stripping reversibility, and improves the cycling stability of aqueous zinc-ion batteries (Fig. S7(B) and Table S1).

4. Conclusion

This study developed a $\text{ZrO}_2\text{-CF}$ 3D scaffold with a three-dimensional porous architecture through electrospinning and thermal treatment. ZrO_2 was uniformly distributed on the fiber surface and within its structure, resulting in a more homogeneous electric field and current density distribution than conventional Zn anodes. This architecture’s “spatial effect” offers a larger specific surface area, ample Zn deposition space, and extensive electronic pathways, ensuring uniform electric field distribution at the anode. In addition, the scaffold’s “anchoring effect,” induced by ZrO_2 , pyridinic N, pyrrolic N, C—C, C—N, C—O, and C—O—Zr and N—Zr—O bridges, facilitates selective interactions with Zn ions, electrons, and protons. These interactions enhance the scaffold’s mechanical strength and conductivity, promoting uniform Zn deposition along the fiber surface while effectively suppressing hydrogen evolution reactions.

The combined “spatial effect” and “anchoring effect” significantly mitigate dendrite formation, reduce the occurrence of “dead Zn,” and suppress side reactions. As a result, the $\text{ZrO}_2\text{-CF}$ electrode demonstrated a high Coulombic efficiency of 98.6 % and maintained stability for over 100 cycles. In full-cell configurations, the $\text{Zn@ZrO}_2\text{-CF//MnO}_2$ system delivered initial capacities of 75 mAh g^{-1} at $1,000 \text{ mA g}^{-1}$ and 124 mAh

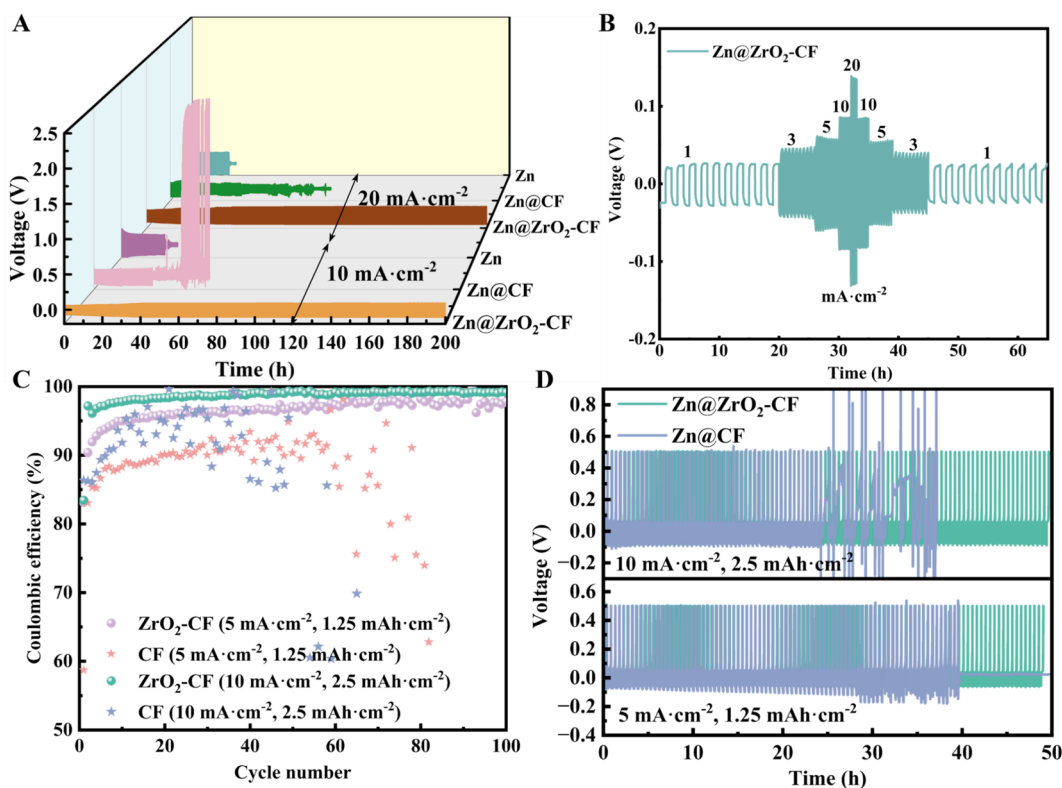


Fig. 8. (A) Charge/discharge voltage profiles of ZrO₂-CF, CF, and Zn symmetric cells at current densities of 10 mA cm⁻² and 20 mA cm⁻². (B) Voltage rate performance curves of the ZrO₂-CF anode at current densities of 1, 3, 5, 10, and 20 mA cm⁻². (C) Coulombic efficiency of ZrO₂-CF and CF anodes under current densities of 10 mA cm⁻² (discharge capacity: 2.5 mAh cm⁻²) and 5 mA cm⁻² (discharge capacity: 1.25 mAh cm⁻²), (D) Potential-time curves of ZrO₂-CF and CF anodes under the same current density and discharge capacity conditions as in (C).

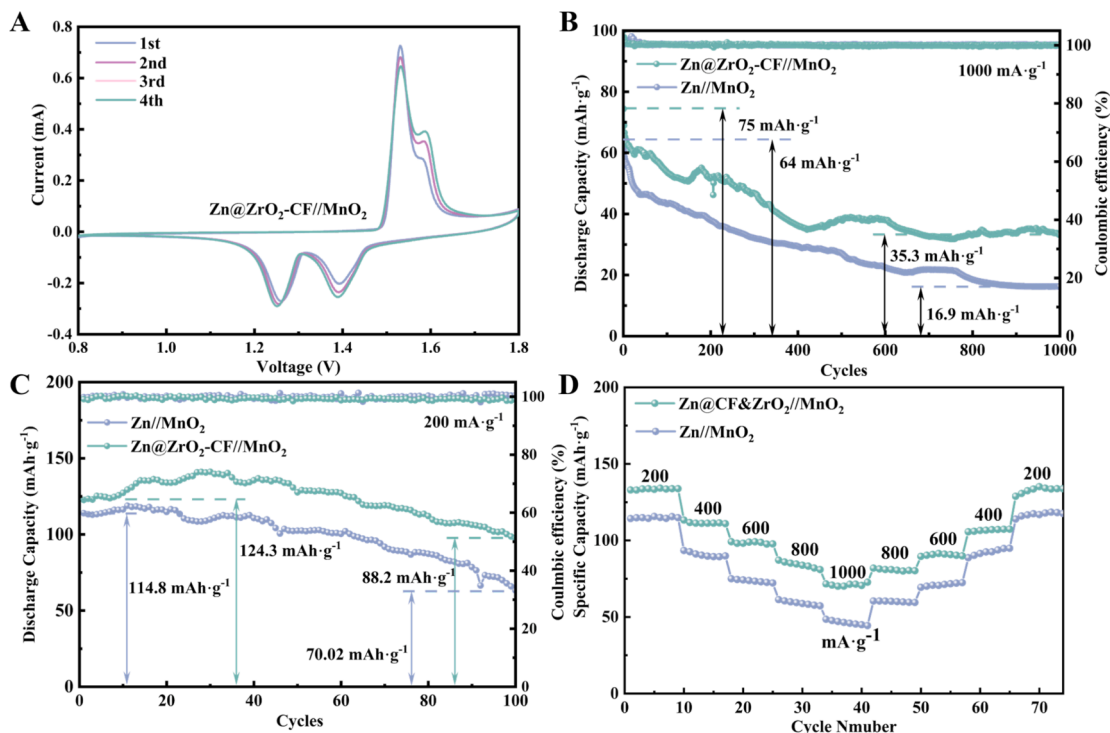


Fig. 9. (A) CV curves of the Zn@ZrO₂-CF//MnO₂ cell during the first four cycles. (B, C) Galvanostatic charge/discharge cycling profiles of Zn@ZrO₂-CF//MnO₂ and Zn//MnO₂ cells at current densities of 1000 mA g⁻¹ (B) and 200 mA g⁻¹ (C). (D) Rate capability curves of Zn@ZrO₂-CF//MnO₂ and Zn//MnO₂ cells at various current densities.

g^{-1} at 200 mA g^{-1} , with capacity retention rates of 47 % and 76.8 % after 100 cycles, respectively. By integrating the “spatial effect” of a 3D architecture with the “anchoring effect” of Zn-philic sites, this study offers novel insights into addressing dendrite formation at its root rather than merely alleviating it. Simultaneously, the scaffold effectively suppresses side reactions, paving the way for broader application scenarios of AZIBs. Furthermore, this approach provides a reference framework for similar electrodeposition and redox processes in industrial applications.

Declaration of Generative AI and AI-assisted technologies in the writing process

In this study, we utilized ChatGPT-4o by OpenAI and Grammarly software by Grammarly Inc. for our manuscript’s language refinement and grammatical corrections. The authors take full responsibility for the content of the publication.

CRedit authorship contribution statement

Jinqiu Ye: Writing – original draft, Validation, Methodology, Data curation. **Tiancheng Ge:** Writing – original draft, Methodology, Investigation, Formal analysis, Conceptualization. **Xin Qu:** Visualization, Validation, Software. **Mohamedazeem M. Mohideen:** Writing – review & editing, Visualization, Resources. **Ce Wang:** Supervision. **Ping Hu:** Supervision. **Yong Liu:** Writing – review & editing, Supervision, Resources, Project administration, Funding acquisition.

Declaration of competing interest

The authors declare that they have no known competing financial interests or personal relationships that could have appeared to influence the work reported in this paper.

Acknowledgment

This work was funded by the National Natural Science Foundations of China (21374008).

Appendix A. Supplementary data

Supplementary data to this article can be found online at <https://doi.org/10.1016/j.cej.2025.159397>.

Data availability

Data will be made available on request.

References

- S. Ha, K.T. Lee, Batteries: converting to long stability, *Nat. Energy* 1 (2016) 16057, <https://doi.org/10.1038/nenergy.2016.57>.
- C. Zhang, Batteries: one size fits all, *Nat. Energy* 1 (2016) 16146, <https://doi.org/10.1038/nenergy.2016.146>.
- Z.-X. Huang, Z.-Y. Gu, Y.-L. Heng, E. Huixiang Ang, H.-B. Geng, X.-L. Wu, Advanced layered oxide cathodes for sodium/potassium-ion batteries: development challenges and prospects, *Chem. Eng. J.* 452 (2023) 139438, <https://doi.org/10.1016/j.cej.2022.139438>.
- M. Xia, J. Zhou, B. Lu, Comprehensive insights into aqueous potassium-ion batteries, *Adv. Energy Mater.* 1 (2024) 2404032, <https://doi.org/10.1002/aenm.202404032>.
- L. Jiang, Y. Lu, C. Zhao, L. Liu, J. Zhang, Q. Zhang, X. Shen, J. Zhao, X. Yu, H. Li, X. Huang, L. Chen, Y.-S. Hu, Building aqueous K-ion batteries for energy storage, *Nat. Energy* 4 (2019) 495–503, <https://doi.org/10.1038/s41560-019-0388-0>.
- S. Feng, L. Fan, H. Zhou, H. Li, S. Yan, W. Zhang, Y. Guo, B. Li, K. Jiang, K. Wang, A Na-Li dual cation liquid metal battery with high electrode utilization and high cycling stability, *Energy Storage Mater.* 73 (2024) 103803, <https://doi.org/10.1016/j.ensm.2024.103803>.
- Y. Liang, Y. Jing, S. Gheyhani, K.-Y. Lee, P. Liu, A. Facchetti, Y. Yao, Universal quinone electrodes for long cycle life aqueous rechargeable batteries, *Nat. Mater.* 16 (2017) 841–848, <https://doi.org/10.1038/nmat4919>.
- S. Li, Z. Huang, F. Liu, X. Gao, J. Guo, S. Li, B. Hong, Y. Lai, Z. Zhang, Unveiling the role of fluorinated interface on anionic redox chemistry in Li-Rich layered oxide cathode materials towards high-energy Li metal batteries, *Energy Storage Mater.* 71 (2024) 103671, <https://doi.org/10.1016/j.ensm.2024.103671>.
- P.G. Bruce, S.A. Freunberger, L.J. Hardwick, J.-M. Tarascon, Li-O₂ and Li-S batteries with high energy storage, *Nat. Mater.* 11 (2012) 19–29, <https://doi.org/10.1038/nmat3191>.
- T. Zhou, R. Huang, Q. Lu, P. Liu, L. Hu, K. Zhang, P. Bai, R. Xu, X. Cao, Z. Sun, S. Duan, R. Liu, Y. Qin, X. Sun, Y. Zhang, Y. Li, Y. Yan, M. Liu, X. Wang, Recent progress and perspectives on highly utilized Zn metal anode - towards marketable aqueous Zn-Ion batteries, *Energy Storage Mater.* 72 (2024) 103689, <https://doi.org/10.1016/j.ensm.2024.103689>.
- Y. Xu, Q. Zhao, C. Lv, Y. Zhu, Y. Zhang, F. Peng, Q. Zhao, Z. Peng, Y. Li, Y. Tang, Regulating H-bonded network of aqueous electrolytes for stable and energy-dense Al-air batteries, *Energy Storage Mater.* 73 (2024) 103772, <https://doi.org/10.1016/j.ensm.2024.103772>.
- H. Liu, Y. Zhang, Q. Xu, W. Han, J. Shen, A carnot battery system integrating ca (OH)₂/CaO thermochemical energy storage and supercritical CO₂ cycles for long-term energy storage and residential heat supply, *Appl. Energy* 377 (2025) 124535, <https://doi.org/10.1016/j.apenergy.2024.124535>.
- Z. Liu, Y. Huang, Y. Huang, Q. Yang, X. Li, Z. Huang, C. Zhi, Voltage issue of aqueous rechargeable metal-ion batteries, *Chem. Soc. Rev.* 49 (2020) 180–232, <https://doi.org/10.1039/C9CS00131J>.
- J. Shin, J.W. Choi, Opportunities and reality of aqueous rechargeable batteries, *Adv. Energy Mater.* 10 (2020) 2001386, <https://doi.org/10.1002/aenm.202001386>.
- L.E. Blanc, D. Kundu, L.F. Nazar, Scientific challenges for the implementation of Zn-Ion batteries, *Joule* 4 (2020) 771–799, <https://doi.org/10.1016/j.joule.2020.03.002>.
- L. Cao, D. Li, T. Pollard, T. Deng, B. Zhang, C. Yang, L. Chen, J. Vatamanu, E. Hu, M.J. Hourwitz, L. Ma, M. Ding, Q. Li, S. Hou, K. Gaskell, J.T. Fourkas, X.-Q. Yang, K. Xu, O. Borodin, C. Wang, Fluorinated interphase enables reversible aqueous zinc battery chemistries, *Nat. Nanotechnol.* 16 (2021) 902–910, <https://doi.org/10.1038/s41565-021-00905-4>.
- A. Naveed, T. Rasheed, B. Raza, J. Chen, J. Yang, N. Yanna, J. Wang, Addressing thermodynamic instability of Zn anode: classical and recent advancements, *Energy Storage Mater.* 44 (2022) 206–230, <https://doi.org/10.1016/j.ensm.2021.10.005>.
- Y. Chu, L. Ren, Z. Hu, C. Huang, J. Luo, An in-depth understanding of improvement strategies and corresponding characterizations towards Zn anode in aqueous Zn-Ions batteries, *Green Energy Environ.* 8 (2023) 1006–1042, <https://doi.org/10.1016/j.gee.2022.04.008>.
- J.-Q. Huang, W.G. Chong, B. Zhang, Tackling the challenges of aqueous Zn-Ion batteries via functional separator design, *J. Power Sources* 594 (2024) 234036, <https://doi.org/10.1016/j.jpowsour.2023.234036>.
- H. Yang, J. Wang, P. Zhang, X. Cheng, Q. Guan, J. Dong, B. Chen, L. Jia, J. Zhang, Y. Zhang, Y. Liu, H. Lin, Dielectric-ion-conductive ZnNb₂O₆ layer enabling rapid desolvation and diffusion for dendrite-free Zn metal batteries, *J. Energy Chem.* 100 (2025) 693–701, <https://doi.org/10.1016/j.jechem.2024.09.010>.
- X. Liu, J. Wang, P. Lv, Y. Zhang, J. Li, Q. Wei, Gel polymer electrolyte based on deep eutectic solvent in flexible Zn-air batteries enables dendrite-free Zn anode, *Energy Storage Mater.* 69 (2024) 103382, <https://doi.org/10.1016/j.ensm.2024.103382>.
- Y.-C. Fu, T.-Y. Lin, Y.-Z. Chen, Te-hybridized zeolitic imidazolate frameworks-derived core-shell design toward dendrite-free Zn anode for long-term Aqueous Zinc-Ion Batteries, *J. Colloid Interface Sci.* 649 (2023) 471–480, <https://doi.org/10.1016/j.jcis.2023.06.141>.
- P. Xu, Q. Zhang, J. Liu, W. Hu, C. Zhong, The analysis of the overall failure of practical Zn–Ni battery, *Chem. Eng. J.* 500 (2024) 157190, <https://doi.org/10.1016/j.cej.2024.157190>.
- J. Chen, W. Zhao, J. Jiang, X. Zhao, S. Zheng, Z. Pan, X. Yang, Challenges and perspectives of hydrogen evolution-free aqueous Zn-Ion batteries, *Energy Storage Mater.* 59 (2023) 102767, <https://doi.org/10.1016/j.ensm.2023.04.006>.
- G. Li, W. Wen, K. Ouyang, Y. Wang, J. Zhu, M. Yang, H. Mi, N. Zhao, P. Zhang, D. Ma, A binary eutectic electrolyte design for high-temperature interface-compatible Zn-Ion batteries, *J. Energy Chem.* 101 (2025) 587–597, <https://doi.org/10.1016/j.jechem.2024.09.068>.
- W. Du, J. Yan, C. Cao, C.C. Li, Electrocrystallization orientation regulation of zinc metal anodes: strategies and challenges, *Energy Storage Mater.* 52 (2022) 329–354, <https://doi.org/10.1016/j.ensm.2022.07.046>.
- Y. Kim, Y. Park, M. Kim, J. Lee, K.J. Kim, J.W. Choi, Corrosion as the origin of limited lifetime of vanadium oxide-based aqueous Zinc Ion batteries, *Nat. Commun.* 13 (2022) 2371, <https://doi.org/10.1038/s41467-022-29987-x>.
- M.K. Aslam, I. Hussain, A.J. Khan, S. Hussain, S.S.A. Shah, A.H. Al-Marzouqi, M. Xu, Unlocking the potential: innovations and strategies for electrolyte optimization in Zn-Ion batteries, *Energy Storage Mater.* 73 (2024) 103851, <https://doi.org/10.1016/j.ensm.2024.103851>.
- L. Jiang, L. Yao, G. Wang, C. Liu, X. Chi, Y. Liu, Long-duration aqueous Zn-Ion batteries achieved by dual-salt highly-concentrated electrolyte with low water activity, *J. Energy Chem.* 101 (2025) 778–785, <https://doi.org/10.1016/j.jechem.2024.09.060>.
- B. Sambandam, H. Lee, S. Kim, A. T. Zikri, K. R. Lestari, S. Lee, aekook Kim, Zn-Anode Stability in Additive Added Perchlorate Electrolyte for Aqueous Zn-MnO₂ Battery, *Journal of Power Sources* 623 (2024) 235413. doi: 10.1016/j.jpowsour.2024.235413.

- [31] Y. Li, L. Zhao, H. Dang, P. Dou, Y. Wu, F. Ran, Designing macromolecular modifiers for Zinc metal batteries, *Mater. Sci. Eng. R. Rep.* 161 (2024) 100844, <https://doi.org/10.1016/j.mser.2024.100844>.
- [32] Y. Qi, M. Xu, Engineering towards stable sodium metal anodes in room temperature sodium-sulfur batteries: challenges progress and perspectives, *Energy Storage Mater.* 72 (2024) 103704, <https://doi.org/10.1016/j.ensm.2024.103704>.
- [33] Z. He, X. Zhu, Y. Song, B. Li, X. Xu, Z. Zhang, N. Zhao, Y. Liu, J. Zhu, L. Wang, L. Dai, H. Tian, Separator functionalization realizing stable zinc anode through microporous metal-organic framework with special functional group, *Energy Storage Mater.* 74 (2025) 103886, <https://doi.org/10.1016/j.ensm.2024.103886>.
- [34] B. Cao, Q. Qu, B. Jiang, T. Zou, S. Zhen, P. Wang, K. Li, J. Zhang, H. Guo, T. Zhang, Zein improved GF separator for dendrite-free aqueous zinc-ion batteries, *J. Mater. Chem. A* 12 (2024) 31185–31194, <https://doi.org/10.1039/D4TA06336H>.
- [35] W. Zhou, M. Chen, Q. Tian, J. Chen, X. Xu, C.-P. Wong, Cotton-Derived cellulose film as a dendrite-inhibiting separator to stabilize the zinc metal anode of aqueous zinc ion batteries, *Energy Storage Mater.* 44 (2022) 57–65, <https://doi.org/10.1016/j.ensm.2021.10.002>.
- [36] Y. Lei, Q. Li, Q. Liu, Y. Zeng, J. Li, W. Huang, F. Wang, S. Zhong, D. Yan, Low-Cost separator with dust-free fabric composite cellulose acetate toward stable dendrite-free aqueous zinc-ion batteries, *Chem. Eng. J.* 479 (2024) 147846, <https://doi.org/10.1016/j.cej.2023.147846>.
- [37] Y. Liu, S. Liu, X. Xie, Z. Li, P. Wang, B. Lu, S. Liang, Y. Tang, J. Zhou, A functionalized separator enables dendrite-free zn anode via metal-polydopamine coordination chemistry, *InfoMat* 5 (2023), <https://doi.org/10.1002/inf2.12374> e12374.
- [38] L. Cheng, W. Li, M. Li, S. Zhou, J. Yang, W. Ren, L. Chen, Y. Huang, S. Yu, J. Wei, Zwitterion modified polyacrylonitrile fiber separator for long-life zinc-ion batteries, *Adv. Funct. Mater.* 34 (2024) 2408863, <https://doi.org/10.1002/adfm.202408863>.
- [39] P.J. Kim, V.G. Pol, High performance lithium metal batteries enabled by surface tailoring of polypropylene separator with a polydopamine/graphene layer, *Adv. Energy Mater.* 8 (2018) 1802665, <https://doi.org/10.1002/aem.201802665>.
- [40] C. Li, Z. Sun, T. Yang, L. Yu, N. Wei, Z. Tian, J. Cai, J. Lv, Y. Shao, M.H. Rummeli, J. Sun, Z. Liu, Directly grown vertical graphene carpets as Janus separators toward stabilized Zn metal anodes, *Adv. Mater.* 32 (2020) 2003425, <https://doi.org/10.1002/adma.202003425>.
- [41] T. Lei, W. Chen, W. Lv, J. Huang, J. Zhu, J. Chu, C. Yan, C. Wu, Y. Yan, W. He, J. Xiong, Y. Li, C. Yan, J.B. Goodenough, X. Duan, Inhibiting polysulfide shuttling with a graphene composite separator for highly robust lithium-sulfur batteries, *Joule* 2 (2018) 2091–2104, <https://doi.org/10.1016/j.joule.2018.07.022>.
- [42] B. Li, Y. Zeng, W. Zhang, B. Lu, Q. Yang, J. Zhou, Z. He, Separator designs for aqueous zinc-ion batteries, *Science Bulletin* 69 (2024) 688–703, <https://doi.org/10.1016/j.scib.2024.01.011>.
- [43] C. Wang, Wenbin Li, Yongkang Wang, Xiao Liu, Congcong Li, Linyan Su, Beibei Yang, An Artificial Sulfonated Polyaniline Coating for High Stable and Dendrite-Free Zinc Anode, *Electrochimica Acta* 500 (2024) 144756, doi: 10.1016/j.electacta.2024.144756.
- [44] K. Wang, B.-Y. Chi, T.-Y. Yang, W.-F. Ren, X.-J. Gao, K.-H. Wang, R.-C. Sun, Natural biopolymers derived kinematic and self-healing hydrogel coatings to continuously protect metallic zinc anodes, *Electrochim. Acta* 489 (2024) 144238, <https://doi.org/10.1016/j.electacta.2024.144238>.
- [45] C. Yang, P. Wootapanit, S. Geng, K. Lolupiman, X. Zhang, Z. Zeng, G. He, J. Qin, Highly reversible Zn anode design through oriented ZnO(002) facets, *Adv. Mater.* 36 (2024) 2408908, <https://doi.org/10.1002/adma.202408908>.
- [46] Z. Bao, Y. Wang, K. Zhang, G. Duan, L. Sun, S. Zheng, B. Luo, Z. Ye, J. Huang, Dual-phase interface engineering via parallel modulation strategy for highly reversible Zn metal batteries, *J. Energy Chem.* 101 (2025) 163–174, <https://doi.org/10.1016/j.jechem.2024.09.053>.
- [47] R.A. Bajwa, U. Farooq, S. Ullah, M. Salman, S. Haider, R. Hussain, Metal-organic framework (MOF) attached and their derived metal oxides (Co, Cu, Zn and Fe) as anode for lithium ion battery: a review, *J. Storage Mater.* 72 (2023) 108708, <https://doi.org/10.1016/j.est.2023.108708>.
- [48] P. Li, J. Ren, C. Li, J. Li, K. Zhang, T. Wu, B. Li, L. Wang, MOF-derived defect-rich CeO₂ as ion-selective smart artificial SEI for dendrite-free Zn-Ion battery, *Chem. Eng. J.* 451 (2023) 138769, <https://doi.org/10.1016/j.cej.2022.138769>.
- [49] W. Zhang, W. Qi, K. Yang, Y. Hu, F. Jiang, W. Liu, L. Du, Z. Yan, J. Sun, Boosting tough metal Zn anode by MOF layer for high-performance zinc-ion batteries, *Energy Storage Mater.* 71 (2024) 103616, <https://doi.org/10.1016/j.ensm.2024.103616>.
- [50] L. Yang, Q. Ma, Y. Yin, D. Luo, Y. Shen, H. Dou, N. Zhu, R. Feng, Y. Kong, A. Yu, B. Cheng, X. Wang, Z. Chen, Construction of Desolvated ionic COF artificial SEI layer stabilized Zn metal anode by in-situ electrophoretic deposition, *Nano Energy* 117 (2023) 108799, <https://doi.org/10.1016/j.nanoen.2023.108799>.
- [51] B. Li, P. Ruan, X. Xu, Z. He, X. Zhu, L. Pan, Z. Peng, Y. Liu, P. Zhou, B. Lu, L. Dai, J. Zhou, Covalent organic framework with 3D ordered channel and multi-functional groups endows Zn anode with superior stability, *Nano-Micro Letters* 16 (2024) 76, <https://doi.org/10.1007/s40820-023-01278-0>.
- [52] T. Mawintorn, K. Lolupiman, N. Kiatwisarnkij, P. Wootapanit, M. Karman, S. Saneewong Na Ayuttay, X. Zhang, P. Wangyao, J. Qin, Fabrication and Characterization of Zinc Anode on Nickel Conductive Cloth for High-Performance Zinc Ion Battery Applications, *Journal of Metals, Materials and Minerals* 34 (2024) 2083, doi: 10.55713/jmnm.v34i3.2083.
- [53] Y. Du, Y. Feng, R. Li, Z. Peng, X. Yao, S. Duan, S. Liu, S.C. Jun, J. Zhu, L. Dai, Q. Yang, L. Wang, Z. He, Zinc-bismuth binary alloy enabling high-performance aqueous zinc ion batteries, *Small* 20 (2024) 2307848, <https://doi.org/10.1002/smll.202307848>.
- [54] Y. Tian, Y. An, J. Feng, Y. Qian, MXenes and their derivatives for advanced aqueous rechargeable batteries, *Mater. Today* 52 (2022) 225–249, <https://doi.org/10.1016/j.mattod.2021.11.021>.
- [55] M. Sun, Y. Sun, N. Wang, L. Hu, X. Ren, C. Jia, Z. Li, 3D hierarchically fractal structure stabilized anode for achieving long-term cycle life of aqueous Zn-Ion batteries, *J. Colloid Interface Sci.* 656 (2024) 440–449, <https://doi.org/10.1016/j.jcis.2023.11.117>.
- [56] M. Zhang, Y. Su, G. Li, B. Tang, S. Zhou, X. Wang, D. Liu, G. Zhu, One-Pot preparation of microporous-polymer protected 3D porous Zn anode to enable advanced aqueous zinc batteries, *J. Power Sources* 589 (2024) 233755, <https://doi.org/10.1016/j.jpowsour.2023.233755>.
- [57] M. Zhang, Y. Deng, Y. Yan, H. Mei, L. Cheng, L. Zhang, Spatially restricted deposition of Zn metal in localized-activation 3D electrode enables long-term stable zinc ion batteries, *Energy Storage Mater.* 65 (2024) 103156, <https://doi.org/10.1016/j.ensm.2023.103156>.
- [58] X.-Y. Fan, H. Yang, B. Feng, Y. Zhu, Y. Wu, R. Sun, L. Gou, J. Xie, D.-L. Li, Y.-L. Ding, Rationally designed In@Zn@In trilayer structure on 3D porous Cu towards high-performance zn-ion batteries, *Chem. Eng. J.* 445 (2022) 136799, <https://doi.org/10.1016/j.cej.2022.136799>.
- [59] Y. Zuo, T. Meng, H. Tian, L. Ling, H. Zhang, H. Zhang, X. Sun, S. Cai, Enhanced H⁺ storage of a MnO₂ cathode via a MnO₂ nanolayer interphase transformed from manganese phosphate, *ACS Nano* 17 (2023) 5600–5608, <https://doi.org/10.1021/acsnano.2c11469>.
- [60] Z. Yan, Y. Zhao, Z. Zhang, G. Li, H. Li, J. Wang, Z. Feng, M. Tang, X. Yuan, R. Zhang, Y. Du, A study on the performance of IrO₂-Ta₂O₅ coated anodes with surface treated Ti substrates, *Electrochim. Acta* 157 (2015) 345–350, <https://doi.org/10.1016/j.electacta.2015.01.005>.
- [61] B. Sui, W. Song, L. Sha, P. Wang, Z. Gong, Y. Zhang, Y. Wu, L. Zhao, J. Tang, F. Shi, Citric acid etched zinc anode surface to improve the stability of aqueous zinc-ion battery, *Solid State Ion.* 405 (2024) 116437, <https://doi.org/10.1016/j.ssi.2023.116437>.
- [62] S. Yang, S. Zhao, S. Chen, Recent advances in electrospinning nanofiber materials for aqueous zinc ion batteries, *Chem. Sci.* 14 (2023) 13346, <https://doi.org/10.1039/d3sc05283d>.
- [63] J. Ye, W. Yu, J. Ge, X. Qu, M.M. Mohideen, C. Wang, P. Hu, Y. Liu, Modification of PLA fibers with novel chitosan-based flame retardants by centrifugal melt electrospinning, *Mater. Today Commun.* 38 (2024) 103353, <https://doi.org/10.1016/j.mtcomm.2024.103353>.
- [64] W. Wang, G. Huang, Y. Wang, Z. Cao, L. Cavallo, M.N. Hedhili, H.N. Alshareef, Organic acid etching strategy for dendrite suppression in aqueous zinc-ion batteries, *Adv. Energy Mater.* 12 (2022) 2102797, <https://doi.org/10.1002/aem.202102797>.
- [65] M. Idrees, S. Batool, J. Cao, M.S. Javed, S. Xiong, C. Liu, Z. Chen, 3D Printed PC/SiOC@Zn hybrid composite as dendrite-free anode for Zn-Ion battery, *Nano Energy* 100 (2022) 107505, <https://doi.org/10.1016/j.nanoen.2022.107505>.
- [66] J. Wang, H. Zhang, L. Yang, S. Zhang, X. Han, W. Hu, In situ implanting 3D carbon network reinforced Zinc composite by powder metallurgy for highly reversible Zn-based battery anodes, *Angew. Chem. Int. Ed.* 63 (2024) e202318149, <https://doi.org/10.1002/anie.202318149>.
- [67] X. Lu, C. Zhao, Z. Liu, Z. Guo, J. Zhang, J. Sun, N. Zhang, High capacity and dendrite-free Zn anode enabled by zincophilic 3D Sn-C nanowire framework, *Chem. Eng. J.* 479 (2024) 147408, <https://doi.org/10.1016/j.cej.2023.147408>.
- [68] C.-C. Chang, R.-J. Yang, A perspective on streaming current in silica nanofluidic channels: poisson-boltzmann model versus poisson-nernst-planck model, *J. Colloid Interface Sci.* 339 (2009) 517–520, <https://doi.org/10.1016/j.jcis.2009.07.056>.
- [69] M.S. Borji, J. Jamaati, M. Bahiraei, Investigating simultaneous effects of temperature, surface heterogeneity and geometry on fluid mixing in electroosmotic flow considering temperature dependent properties by nernst-planck poisson method, *Commun. Nonlinear Sci. Numer. Simul.* 121 (2023) 107238, <https://doi.org/10.1016/j.cnsns.2023.107238>.
- [70] G. Xing, K. Masuda, T. Tadano, Y. Miura, Chemical-substitution-driven giant anomalous hall and nernst effects in magnetic cubic heusler compounds, *Acta Mater.* 270 (2024) 119856, <https://doi.org/10.1016/j.actamat.2024.119856>.
- [71] S. Zhang, X. Dai, W. Hao, L. Liu, Y. Ma, Y. Zou, J. Zhu, C. Di, A first-principles study of the nernst effect in doped polymer, *Chin. Chem. Lett.* 35 (2024) 109837, <https://doi.org/10.1016/j.ccllet.2024.109837>.
- [72] N. Dhiman, B. Joshi, S.R. Yenumala, O. Singh, R. Bal, A. Ray, B. Sarkar, Greener production of styrene via low-temperature dehydration of phenethyl alcohol over co-supported P/ZrO₂, *Chem. Eng. J.* 480 (2024) 148005, <https://doi.org/10.1016/j.cej.2023.148005>.
- [73] F. Xu, X. Meng, R. Zhao, D. Jin, W. Dai, D. Yang, Z. Xin, Fe₂O₃@ZrO₂ catalyst derived from MOF-on-MOF for direct CO₂ hydrogenation to light olefins, *Chem. Eng. J.* 494 (2024) 152926, <https://doi.org/10.1016/j.cej.2024.152926>.
- [74] X. Song, X. Chen, W. Chen, T. Ao, ZrO₂ Nanoparticles embedded in biochar modified with layered double oxides nanosheets for phosphorus removal by capacitive deionization, *Sep. Purif. Technol.* 328 (2024) 125117, <https://doi.org/10.1016/j.seppur.2023.125117>.
- [75] J. P. Cedric, *NIST Data Resources for X-Ray Photoelectron Spectroscopy*. NIST Data Resources for X-Ray Photoelectron Spectroscopy. <https://www.nist.gov/publications/nist-data-resources-x-ray-photoelectron-spectroscopy> (accessed 2024-11-21).
- [76] W. Geng, P. Song, X. Cao, L. Duan, NiO/ZrO₂ hollow microspheres derived from bimetallic Ni/Zr-MOFs for fast and sensitive detection of triethylamine, *J. Alloy. Compd.* 1006 (2024) 176277, <https://doi.org/10.1016/j.jallcom.2024.176277>.